

Application of Dual Modality Contrast Agent Combined with Multi-Scale Representation in Ultrasound-Magnetic Resonance Imaging Registration Scheme

Mo Hou^{1,*}, Weiyu Kevin Chiang^{2,*}, Weiqiang Hong¹, Maoyun Yang¹ and Wenhua Yu^{3,4}

¹School of Computer Science and Technology, Jiangsu Normal University, Xuzhou, 221116, China

²College of Business, City University of Hong Kong, Hong Kong, 999077, China

³School of Mathematics Science, Jiangsu Normal University, Xuzhou, 221116, China

⁴Key Laboratory of Education Big Data Science and Engineering, Jiangsu Normal University, Xuzhou, 221116, China

*Corresponding Authors: Mo Hou. Email: houmo@jsnu.edu.cn; Weiyu Kevin Chiang. Email: wchiang@cityu.edu.hk

Received: 30 March 2020; Accepted: 05 June 2020

Abstract: To achieve the image registration/fusion and perfect the quality of the integration, with dual modality contrast agent (DMCA), a novel multi-scale representation registration method between ultrasound imaging (US) and magnetic resonance imaging (MRI) is presented in the paper, and how DMCA influence on registration accuracy is chiefly discussed. Owing to US's intense speckle noise, it is a tremendous challenge to register US with any other modality images. How to improve the algorithms for US processing has become the bottleneck, and in the short term it is difficult to have a breakthrough. In that case, DMCA is employed in both US and MRI to enhance the region of interest. Then, because multi-scale representation is a strategy that attempts to diminish or eliminate several possible local minima and lead to convex optimization problems to be solved quickly and more efficiently, a multi-scale representation Gaussian pyramid based affine registration (MRGP-AR) scheme is constructed to complete the US-MRI registration process. In view of the above-mentioned method, the comparison tests indicate that US-MRI registration/fusion may be a remarkable method for gaining high-quality registration image. The experiments also show that it is feasible that novel nano-materials combined with excellent algorithm are used to solve some hard tasks in medical image processing field.

Keywords: US; MRI; accuracy; registration; DMCA; MRGP-AR

1 Introduction

Because US is high efficient, easy to operate and maintenance, it is widely used in clinical application of the city and the countryside. At present, US is greatly improved owing to the use of contrast agents [1–4]. However, because of imaging principle of US, the quality of US is very general compared its contrast and resolution with that of MRI or computed tomography (CT). MRI is another applied generally imaging modality with desired soft-tissue contrast and high-quality spatial contrast and resolution; in addition, in



This work is licensed under a Creative Commons Attribution 4.0 International License, which permits unrestricted use, distribution, and reproduction in any medium, provided the original work is properly cited.

particular MRI can offer functional information required by the clinical diagnosis. The fatal defect of MRI is that it can't provide real-time motion-related images.

To sum up, no single imaging modality possesses all the virtues fulfilling various clinical needs, and various imaging modalities own their respective merits and defects in clinical application. Under many circumstances, it is complimentary between MRI and US. Accordingly, and it is ideal to fuse US with MRI. To fuse US and MRI together, firstly US-MRI registration is needed. For the moment, Owing to US's strong noise and unclear background, to register US with any other imaging modality is a significant challenge. Though researchers have made great efforts to improve algorithms for medical image registration, they made very little progress in this field [5–10]. We have done preliminary work on MRI-US registration/fusion based on DMCA, and have obtained some results [11–14].

At present many scholars have shown interest in DMCA and have made great progress. The above-mentioned DMCA is the dual-modality contrast agent, which holds contrast function property for both US and MRI at the same time. Superparamagnetic iron oxide nanoparticles (SPIO) can be used as an efficient contrast agent for MRI, while microbubbles can be used as a powerful contrast agent for US. The combination of SPIO and microbubbles, DMCA, can be used as the dual-modality contrast agent for both US and MRI because the DMCA can enhance the merits and decrease the defects of SPIO or microbubbles, respectively. Wang et al. [15,16] developed a new class of uniform biodegradable yolk-shell $\text{Fe}_3\text{O}_4@PFH@PMAA\text{-DOX}$ microspheres as US/MRI dual-modality imaging contrast agents and drug delivery system, and the multifunctional biodegradable microspheres are safer for normal tissues and more beneficial in actual clinical applications. Song et al. [17,18] prepared superparamagnetic self-assembled microbubbles consisting of "Poly(acrylic acid)-Iron oxide nanoparticles-Polyamine" sandwich-like shells and tetradecafluorohexane cores were fabricated by a template-free self-assembly approach, showing great potential as US/MRI dual contrast agents. Morch et al. [19] developed nanoparticle-stabilized microbubbles for multimodal imaging and drug delivery, showing that these microbubbles can act as contrast agents for conventional ultrasound imaging. Successful encapsulation of iron oxide nanoparticles inside the poly butyl cyanoacrylate nanoparticles is demonstrated, potentially enabling the nanoparticle-microbubbles to be used as MRI/US contrast agents. Wang et al. [20] developed a dual-enzyme-loaded multifunctional hybrid nanogel probe (SPIO@GCS/acryl/biotin-CAT/SOD-gel, or SGC) for dual-modality pathological responsive US and enhanced T2-weighted MRI. This probe is composed of functionalized superparamagnetic iron oxide particles, a dual enzyme species (catalase and superoxide dismutase), and a polysaccharide cationic polymer glycol chitosan gel. Wu et al. [21] adopted a premix membrane emulsification (PME) method to prepare uniform PEGylated poly (lactic-co-glycolic acid) microcapsules with superparamagnetic Fe_3O_4 nanoparticles embedded in the shell ($\text{Fe}_3\text{O}_4@PEG\text{-PLGA}$ MCs) for US/MRI.

Multimodal contrast agent (MMCA) or DMCA has been used preliminarily in clinical practice. Zheng et al. [22] introduced an MMCA, which may serve as a valuable tool for cardiovascular imaging as well as image registration and guidance applications in radiation therapy. Kuznetsova et al. [23] assessed the performance of structure-guided deformable image registration (SG-DIR) relative to rigid registration and DIR using TG-132 recommendations. The assessment was carried out for image registration of operation planning CT and MRI scans with Primovist contrast agent obtained post stereotactic body radiation therapy. Piskunowicz et al. [24] presented some cases of pediatric patients treated in oncological departments, with the use of ultrasound contrast agents, the examination had a considerable influence on the diagnostic and therapeutic process. It showed that imaging with contrast agents could help solve some clinical problems when other diagnostic methods failed. Literature review shows that registration based on MMCA OR DMCA is still rarely studied.

The important contribution of the paper is the introduction of MRGP-AR algorithm combined with the above-mentioned novel nano-materials DMCA to US-MRI registration [21,25,26], and focuses on the research of how DMCA influences on registration accuracy between US and MRI. Employing DMCA prepared by Yang et al. [1], based on MRGP-AR scheme, this paper carries out the research on registration accuracy of US-MRI, and gets a conclusion that with the use of DMCA, the proposed MRGP-AR method works well. The rest of the paper is arranged as shown below: US-MRI registration scheme (MRGP-AR) is demonstrated in Section 2. Section 3 provides comparison experiments on registration accuracy with/without DMCA, and discusses the experimental results, while Section 4 summarizes our paper.

2 Registration Method

During registration process, it is essential for interpolation transformation of floating image, and the diagram of cubic convolution interpolation is given in Fig. 1. In the registration process, to enhance the region of interest, DMCA is injected into phantom, and US and MRI with/without DMCA are obtained. Then MRGP-AR scheme is constructed to complete the US-MRI registration process. Finally, affine transformation parameters are estimated and used to register the US, and how DMCA influence on registration accuracy is chiefly discussed by multiple comparison experiments with/without DMCA. The diagram of the proposed registration method MRGP-AR combined with/without DMCA is shown in Fig. 2, and multiscale scheme is introduced as shown in Fig. 3. The basic steps of MRGP-AR are as followed:

Step 1: Build the multi-scale representation by cubic convolution interpolation at different scales (Section 2.1).

Step 2: Carry on affine registration at the most coarse scale π_0 (Section 2.2), get the solution u_{π_0} .

Step 3: For $i = 1, \dots, n$, at each scale π_i , carry on affine registration and compute the similarity measure for evaluation of the registration approach, $u_{\pi_{i-1}}$ as the initial guess, then get the solution u_{π_i} .

Step 4: Let \tilde{u} be the solution at the final scale, that is, the affine transformation parameters are estimated $\tilde{u} = u_{\pi_n}$.

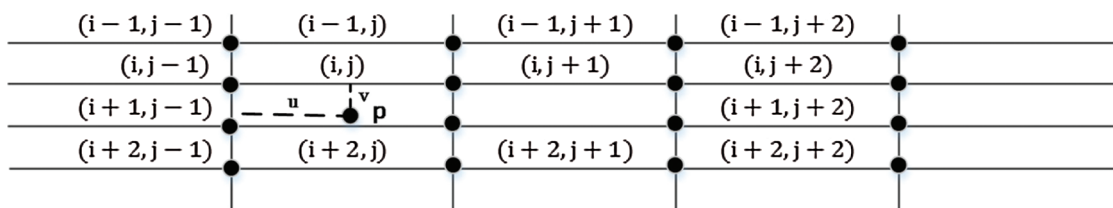


Figure 1: Diagram of cubic convolution interpolation

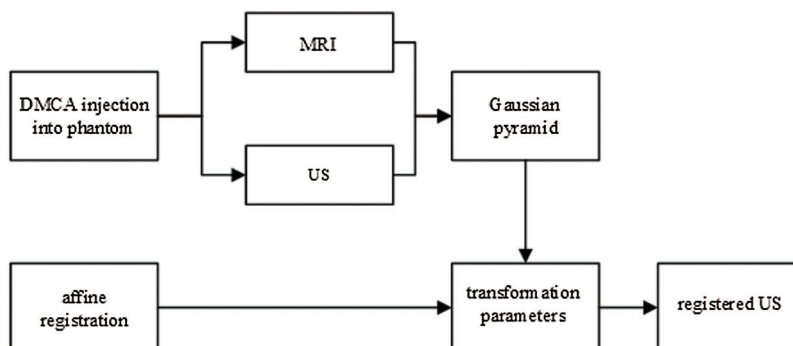


Figure 2: Flow chart of the proposed MRGP-AR method combined with DMCA

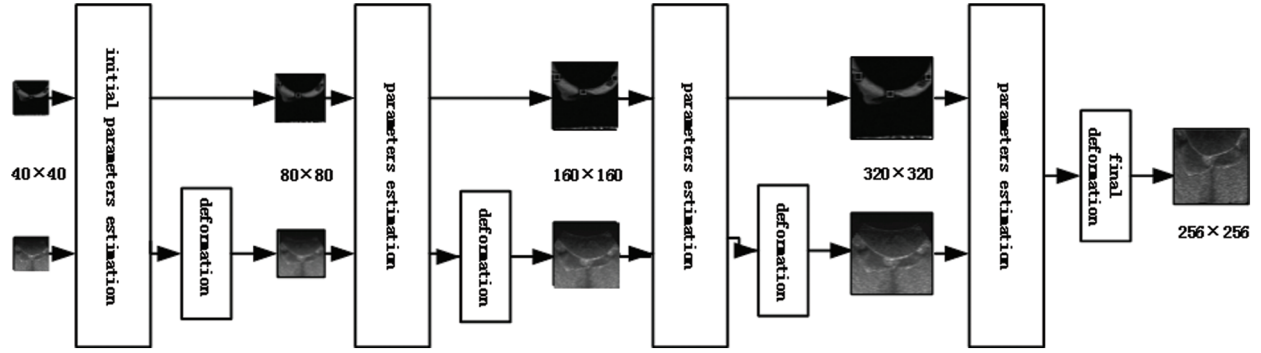


Figure 3: Flow chart of multi-scale Gaussian pyramid algorithm

2.1 Cubic Convolution Interpolation Based Multi-Scale Representation

To build Gaussian pyramid, down-sampling is needed. At each scale registration, cubic convolution interpolation is introduced to transform the floating image. On the basis of grey scales of all the sixteen pixels in a small neighboring area around the reverse transformation point p , weighted mean value of p is computed according to a certain weighting coefficients, and the gray value of the inverse transform point is interpolated. Schematic diagram of cubic convolution interpolation is shown as Fig. 1.

Suppose the floating image is mapped to the reference image in reverse direction, a transformation point is obtained, and its coordinates are $(i + u, j + v)$, where i and j are positive integers, u and v are pure decimals of the $[0, 1)$ interval. The value of $f(i + u, j + v)$ can be determined by the gray values of the 16 pixels of the p centered neighborhood in the original (or reference) image. The formula is followed as shown in (1).

$$f(i + u, j + v) = A \times B \times C, \quad (1)$$

where

$$A = [s(1 + v) \quad s(v) \quad s(1 - v) \quad s(2 - v)], \quad (2)$$

$$B = \begin{bmatrix} f(i - 1, j - 1) & f(i - 1, j) & f(i - 1, j + 1) & f(i - 1, j + 2) \\ f(i, j - 1) & f(i, j) & f(i, j + 1) & f(i, j + 2) \\ f(i + 1, j - 1) & f(i + 1, j) & f(i + 1, j + 1) & f(i + 1, j + 2) \\ f(i + 2, j - 1) & f(i + 2, j) & f(i + 2, j + 1) & f(i + 2, j + 2) \end{bmatrix}, \quad (3)$$

$$C = \begin{bmatrix} s(1 + u) \\ s(u) \\ s(1 - u) \\ s(2 - u) \end{bmatrix}, \quad (4)$$

$$s(w) = \begin{cases} 1 - 2|w|^2 + |w|^3 & |w| < 1 \\ 4 - 8|w| + 5|w|^2 - |w|^3 & 1 \leq |w| < 2. \\ 0 & |w| \geq 2. \end{cases} \quad (5)$$

In (5), $s(w)$ is a weighted interpolation coefficient function.

2.2 Affine Registration

We introduce a particular rigid-like type of affine transformation φ , which is a composition of scaling, rotation and translations, defined by (6).

$$\begin{pmatrix} x_1 \\ y_1 \end{pmatrix} = \varphi \begin{pmatrix} x_0 \\ y_0 \end{pmatrix} = \omega_0 \begin{pmatrix} \cos(\theta) & \sin(\theta) \\ -\sin(\theta) & \cos(\theta) \end{pmatrix} \begin{pmatrix} x_0 \\ y_0 \end{pmatrix} + \begin{pmatrix} \Delta x \\ \Delta y \end{pmatrix}, \quad (6)$$

where φ is the solution of the following optimization problem as shown in (7).

$$\min_{\varphi} \frac{1}{2} \|\text{MRI}_{\pi_i} - \varphi(\text{US}_{\pi_i})\|^2. \quad (7)$$

In (6), $\begin{pmatrix} x_0 \\ y_0 \end{pmatrix}$ and $\begin{pmatrix} x_1 \\ y_1 \end{pmatrix}$ are initial coordinate and transformation coordinate, respectively. ω_0 represents the scale, which is set to 1 and ignored in the next sections. θ is the rotation angle. Δx and Δy denote the translations on the x-axes and y-axes, respectively.

At coarse scales, the corresponding input representations preserve only the main and global features of the images, and successively, at finer scales these representations contain more and more details. At coarse scales, because of down-sampling, the size of start images is relatively small, and the global registration parameters are relatively easy to be estimated, and then the solution of the registration problem at one scale is the starting guess for the registration problem defined at the next finer scale, where the representation of the data (reference and floating images) is obtained with the next scale and shows more details. This multi-scale representation is a strategy that attempts to diminish or eliminate several possible local minima and lead to convex optimization problems to be solved quickly and more efficiently [27–29].

3 Results and Discussion

Phantom and DMCA are made and acquired from Jiangsu Key Laboratory for Biomaterials and Devices. Phantom is prepared from glycerol, agar and water ratio of 3:4:90, in which a “U” shaped silicone tube is “vertically” set to sit in the agar phantom. The production process of DMCA can be consulted from relevant literatures [1,2,12], and DMCA can negatively boost MRI T2-weighted (T2*WI) imaging signal; on the contrary, it can positively reinforce ultrasound backscattering echo intensity and boost the contrast and brightness of US.

With/without DMCA, for US, the phantom is imaged by using the GE LOGIQ3 PRO equipment with a 4 MHz ultrasound transducer; For MRI, the phantom’s T2*WI imaging is carried out by using a 0.3 T magnetic resonance equipment (AIRISII, Hitachi Ltd., JAPAN).

Two-dimensional MRI is used as reference plane, while an image generated by an affine transformation of a parameter $\alpha = (\Delta x, \Delta y, \Delta\theta)$ based on a two-dimensional ultrasonic plane is used as a floating image, and comparison tests of registration accuracy with/without DMCA are carried on. For the parameter α , the coordinate system is defined as shown in Fig. 4. Δy is vertical and upward on Y-axes direction, Δx is horizontal and left on X-axes direction, and $\Delta\theta$ is anticlockwise in rotation direction, respectively. For the parameter α , the unit of Δx and Δy is pixel, and the unit of $\Delta\theta$ is degree, namely $\frac{\pi}{180}$. In the following experiments, α is set to (3, 3, 3), (8, 8, 8), (11, 11, 11) and (15, 15, 15), respectively.

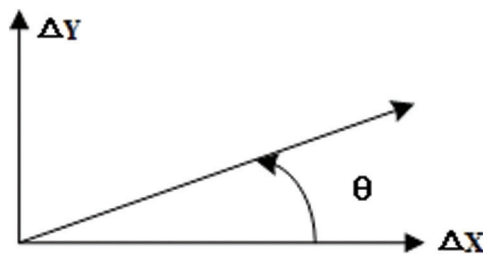


Figure 4: The coordinate system on parameter α

3.1 Registration Results with the Proposed Improved Affine Transformation (MRGP-AR)

Using MRGP-AR, comparison results of registration accuracy without/with DMCA are as shown in Figs. 5 and 6, respectively, and the registration accuracy comparison results, namely corresponding transformation parameters, are computed quantitatively as shown in Tab. 1.

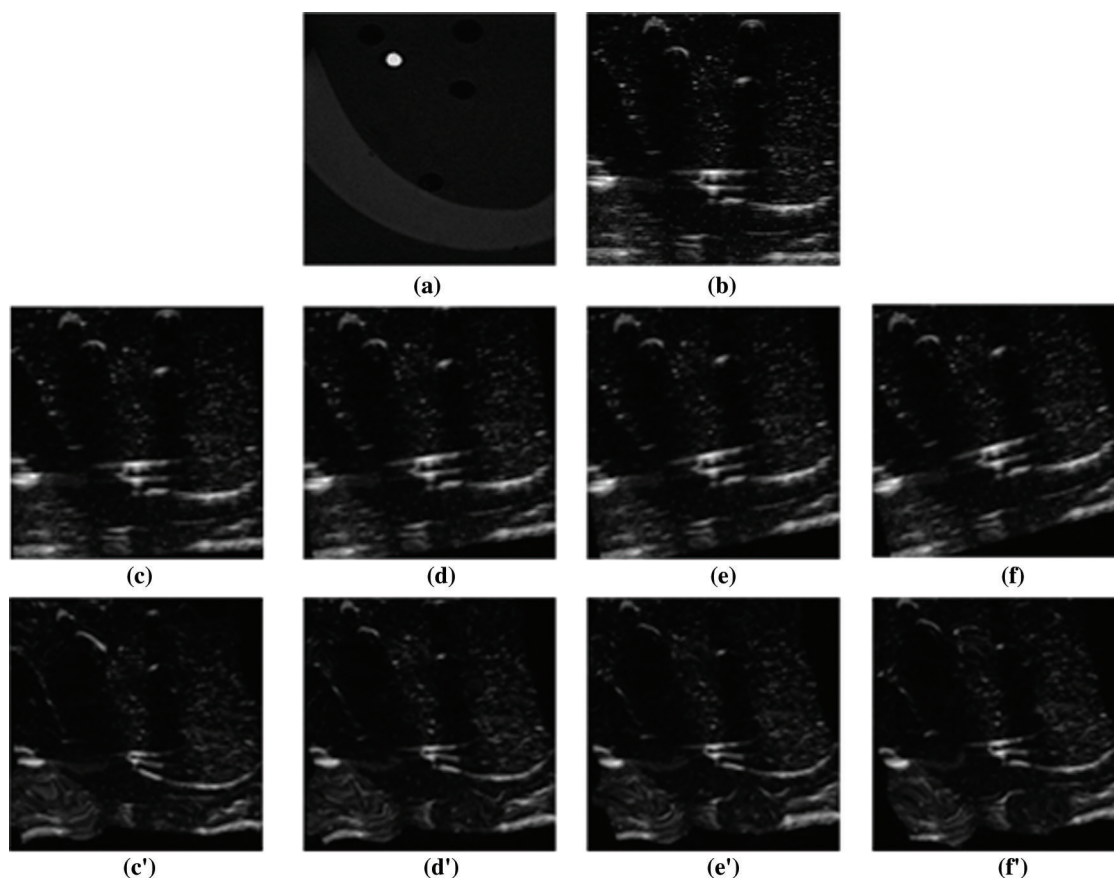


Figure 5: Comparison results of registration accuracy without DMCA. (a) MRI, (b) US, (c)–(f) are floating images with affine transformation for US, and transformation parameters are (3, 3, 3), (8, 8, 8), (11, 11, 11) and (15, 15, 15), respectively. (c')–(f') are corresponding registration images of (c)–(f), respectively

The MRI or US imaging of a “U” shaped silicone tube in the phantom is called region of interest (ROI). Obviously, the ROI of Fig. 6a is darker than that of Fig. 5a because DMCA can negatively enhance MRI T2*WI imaging; similarly, the ROI of Fig. 6b is brighter than that of Fig. 5b because DMCA can positively boost the contrast and brightness of US. Besides, intuitively, the detail information the ROI of Figs. 6a and 6b is more abundant than that of Figs. 5a and 5b.

From Tab. 1, when α is set to (3, 3, 3), (8, 8, 8), (11, 11, 11) and (15, 15, 15), respectively, without DMCA, the transformation parameters (0.8864, 1.6095, 3.4972), (1.9466, 3.3307, 4.9054), (4.2087, 6.9406, 6.7736) and (7.8865, 6.7304, 5.4408) are solved, respectively; with DMCA, the transformation parameters (2.4863, 2.6590, 2.6024), (8.7058, 6.9075, 6.7746), (9.8846, 9.7603, 8.7094) and (12.8875, 12.9041, 10.2507) are worked out, respectively.

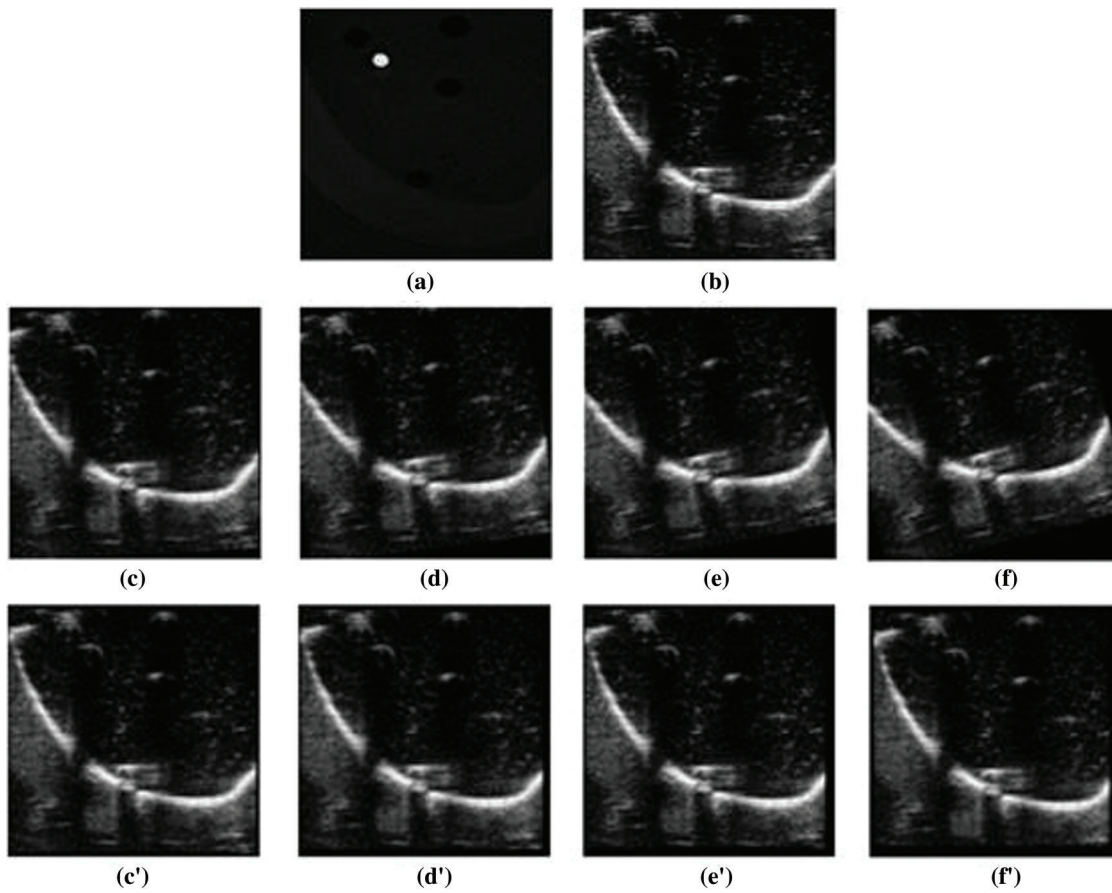


Figure 6: Comparison results of registration accuracy with DMCA. (a) MRI, (b) US, (c)–(f) are floating images with affine transformation for US, and transformation parameters are (3, 3, 3), (8, 8, 8), (11, 11, 11) and (15, 15, 15) respectively. (c')–(f') are corresponding registration images of (c)–(f), respectively

Table 1: Registration accuracy comparison results (MRGP-AR)

Categories	Initial affine transformation parameters			Categories	Calculated transformation parameters			
	Δx	Δy	$\Delta \theta$		Δx	Δy	$\Delta \theta$	
Before registration	without DMCA	3	3	3	After registration	0.8864	1.6095	3.4972
		8	8	8		1.9466	3.3307	4.9054
		11	11	11		4.2087	6.9406	6.7736
		15	15	15		7.8865	6.7304	5.4408
	with DMCA	3	3	3	2.4863	2.6590	2.6024	
		8	8	8	8.7058	6.9075	6.7746	
		11	11	11	9.8846	9.7603	8.7094	
		15	15	15	12.8875	12.9041	10.2507	

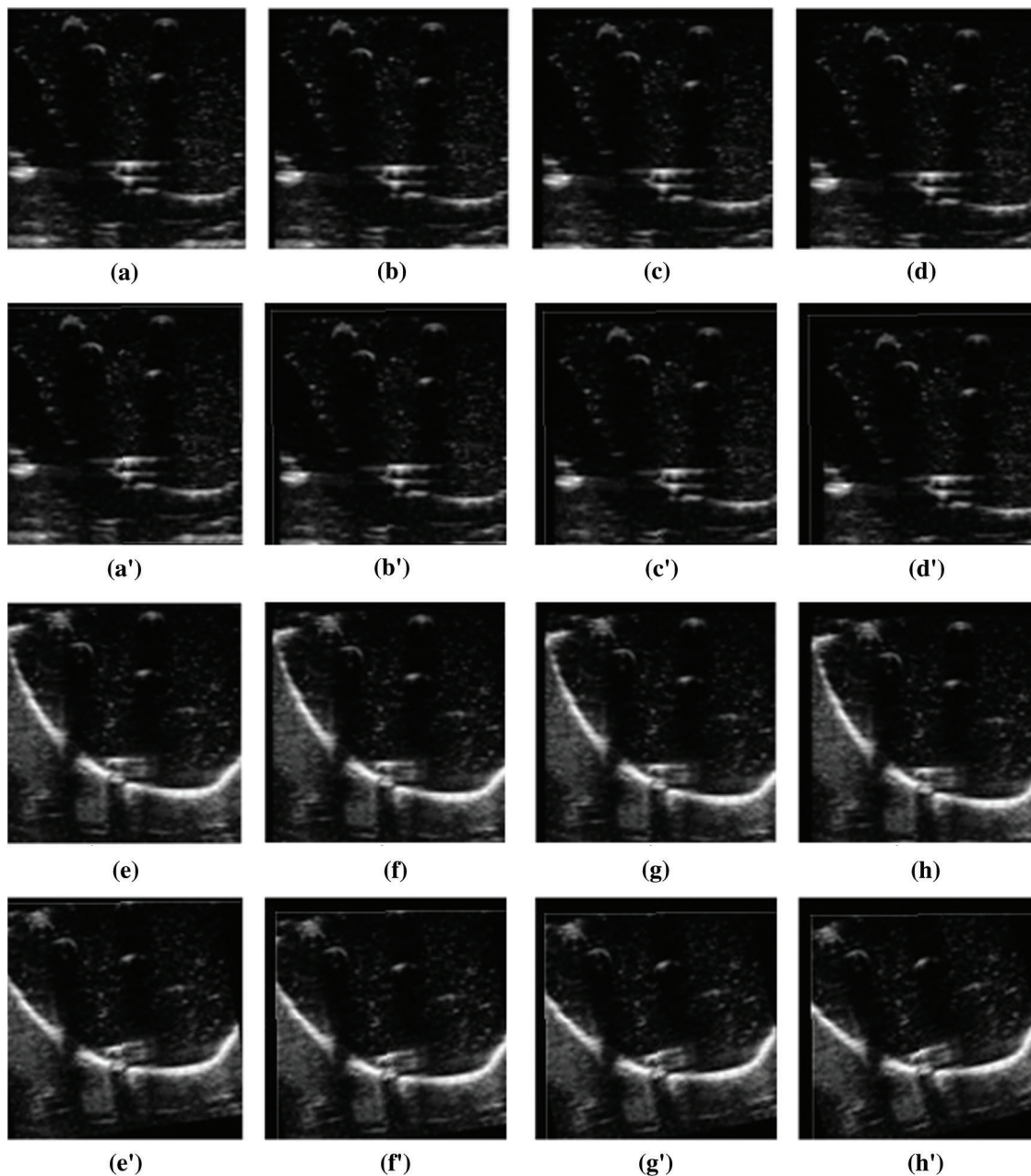


Figure 7: Comparison results of registration accuracy of TAT without/with DMCA. (a)–(d) are floating images with affine transformation for US (without DMCA), and transformation parameters are (3, 3, 3), (8, 8, 8), (11, 11, 11) and (15, 15, 15), respectively. (a')–(d') are corresponding registration images of (a)–(d), respectively. (e)–(f) are floating images with affine transformation for US (with DMCA), and transformation parameters are (3, 3, 3), (8, 8, 8), (11, 11, 11) and (15, 15, 15), respectively. (e')–(f') are corresponding registration images of (e)–(f), respectively

Evidently, by qualitative and quantitative analysis, the following conclusion can be obtained from [Tab. 1](#), with DMCA, for MRGP-AR the better registration accuracy and less deviation can be obtained compared with not using DMCA.

Table 2: Registration accuracy comparison results (TAT)

Categories		Initial affine transformation parameters			Categories		Calculated transformation parameters		
		Δx	Δy	$\Delta \theta$			Δx	Δy	$\Delta \theta$
Before registration	without DMCA	3	3	3	After registration	without DMCA	0.7855	1.5487	4.3232
		8	8	8			1.4264	2.6603	4.4189
		11	11	11			3.1849	3.5634	6.5693
		15	15	15			6.0215	5.9163	5.0041
	with DMCA	3	3	3	With DMCA	1.5992	2.2584	2.0400	
		8	8	8		9.8421	5.8769	5.1844	
		11	11	11		9.4166	5.0926	8.1796	
		15	15	15		10.0084	8.1667	8.9700	

3.2 Registration Results with Traditional Affine Transformation (TAT)

Using TAT [30–33], comparison results of registration accuracy without/ with DMCA are as shown in Fig. 7, respectively, and the corresponding transformation parameters are computed as shown in Tab. 2.

From Tab. 2, when α is set to (3, 3, 3), without/with DMCA, the transformation parameters (0.7855, 1.5487, 4.3232) and (1.5992, 2.2584, 2.04) are computed, respectively. When α are set to (8, 8, 8), (11, 11, 11) and (15, 15, 15), respectively, without DMCA, the transformation parameters (1.4264, 2.6603, 4.4189), (3.1849, 3.5634, 6.5693) and (6.0215, 5.9163, 5.0041) are solved, respectively; with DMCA, the transformation parameters (9.8421, 5.8769, 5.1844), (9.4166, 5.0926, 8.1796) and (10.0084, 8.1667, 8.9700) are worked out, respectively.

Obviously, with DMCA, for TAT the better registration accuracy and less deviation can be obtained compared with not using DMCA. For example, before registration, when α is set to (3, 3, 3), the computed transformation parameters are (0.7855, 1.5487, 4.3232) and (1.5992, 2.2584, 2.0400) without/ with DMCA as shown in Tab. 2, respectively.

Table 3: Comparison results of angle errors of optical flow field algorithm

Categories	Angle errors		
	Δx	Δy	θ_{err}
without DMCA	3	3	1.4531
	8	8	1.4767
	11	11	1.4733
	15	15	1.4716
with DMCA	3	3	1.3637
	8	8	1.4029
	11	11	1.4080
	15	15	1.4048

3.3 Registration Results with Optical Flow Field Method

Optical flow field method is introduced to further to measure the error between the displacement vector calculated by the optical flow field algorithm and the known displacement vector, the quantitative index of angle error is introduced as shown in (8) [34–37].

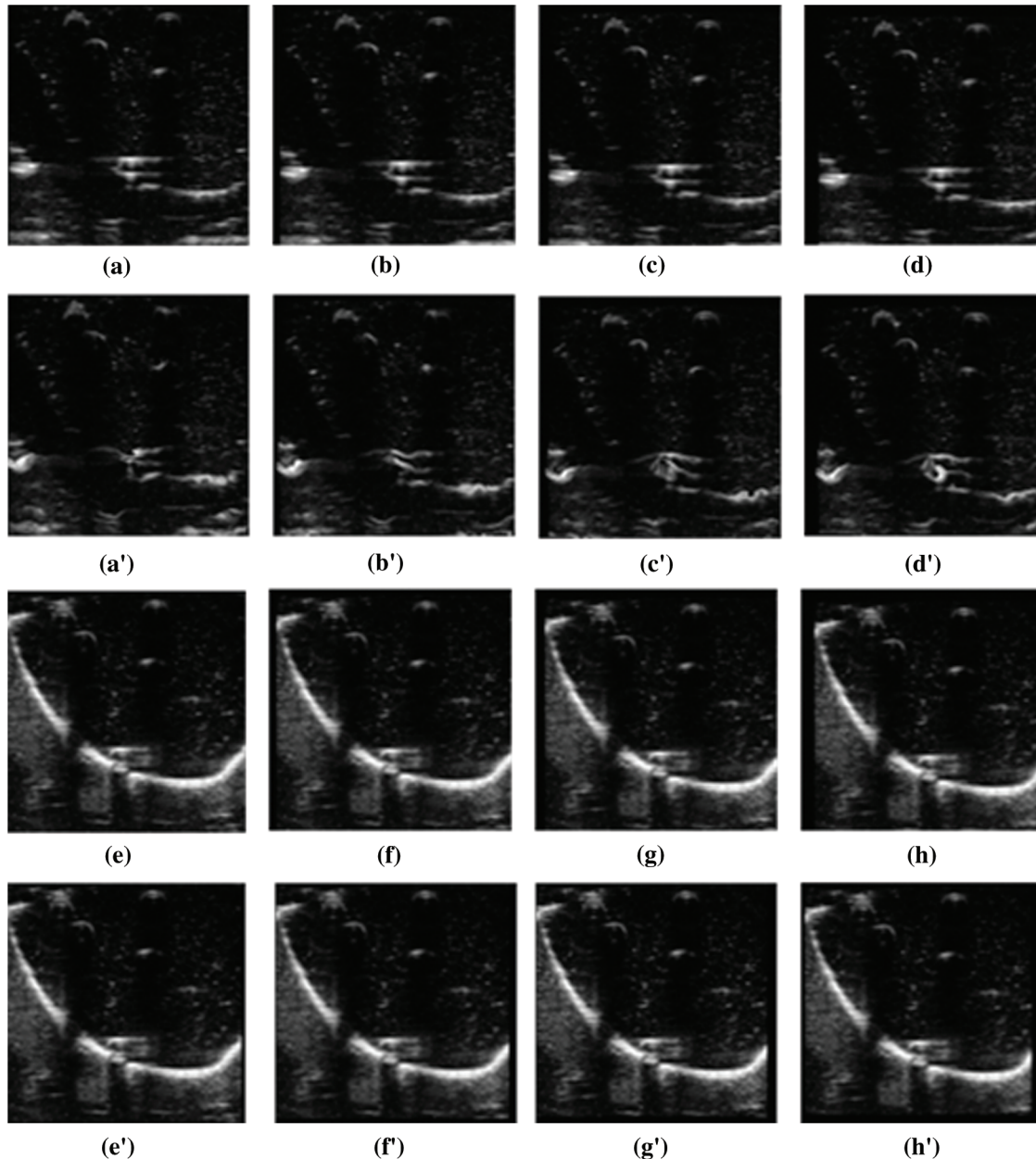


Figure 8: Comparison results of angle errors of optical flow field algorithm without/with DMCA. (a)–(d) are floating images with affine transformation for US (without DMCA), and transformation parameters are (3, 3), (8, 8), (11, 11), and (15, 15), respectively. (a')–(d') are corresponding registration images of (a)–(d), respectively. (e)–(f) are floating images with affine transformation for US (with DMCA), and transformation parameters are (3, 3), (8, 8), (11, 11), and (15, 15), respectively. (e')–(f') are corresponding registration images of (e)–(f), respectively

$$\theta_{err} = \arccos\left(\frac{\langle U, \hat{U} \rangle}{\|U\| \cdot \|\hat{U}\|}\right), \quad (8)$$

where $U = (u, v)$, $\hat{U} = (\hat{u}, \hat{v})$.

Because the algorithm of optical flow field is not sensitive to rotation, in the following experiments, only the parameters Δx and Δy of α are considered, and set to (3, 3), (8, 8), (11, 11), and (15, 15), respectively. Comparison results of angle errors of optical flow field algorithm with/without DMCA are shown in Fig. 8, and the corresponding angle error is quantitatively calculated in Tab. 3.

From Fig. 8 and Tab. 3, the angle error obtained without using DMCA is obviously larger than that obtained with DMCA, which shows that DMCA is beneficial to optical flow field registration algorithm. For example, with DMCA, the angle errors are 1.3637, 1.4029, 1.4080 and 1.4048, respectively. Without DMCA, the angle errors are 1.4531, 1.4767, 1.4733 and 1.4716, respectively.

Briefly speaking, from Tabs. 1–3, with the increase of the parameters α values from (3, 3, 3) to (15, 15, 15), no matter whether MRGP-AR, TAT or optical flow field method is used, and no matter whether DMCA is added or not, there is a growing trend of the deviations between the set parameters and the corresponding solved transformation parameters because the greater the parameters are set, the more difficult the registration is. The fundamental cause is that as the offset between the floating image and the reference image increases, search space increases during registration. The registration process is more likely to fall into local optimum, resulting in the final solution is not ideal.

Comparison between Tabs. 1 and 2, no matter whether DMCA is added or not, for MRGP-AR the better registration accuracy and less deviation can be obtained compared with that of TAT. The fundamental cause lies in multi-scale representation based the construction of Gaussian pyramid. By the above coarse-to-fine Gaussian pyramid, at the coarse level, we can roughly calculate the transformation parameters as a whole, and the computed affine parameters are used as initialization parameters at fine level. Beginning from the top story, calculation is conducted downward story by story, the computed affine transformation parameters successive approximated of real values, which can also be intuitively seen in Fig. 3. To sum up, without DMCA, for MRGP-AR, TAT and optical flow field method, the calculated registration accuracy is not ideal. However, the proposed method, MRGP-AR combined with DMCA, higher registration accuracy is achieved compare to that using TAT or optical flow field method with DMCA. It can also be intuitively seen from Figs. 5–8 that by using DMCA, the contrast and brightness of US and MRI are improved compared with not using DMCA, which is beneficial to subsequent registration.

4 Conclusions

Based on MRGP-AR algorithm combined with the novel nano-materials DMCA, US-MRI registration is carried out, and some conclusions are drawn as follows.

Firstly, for US-MRI registration, large amount of data, long running time, and easy to fall into local minimum need to be solved urgently. The multi-scale representation is a strategy that attempts to diminish or eliminate several possible local minima, and lead to convex optimization problems to be solved quickly and more efficiently. The multi-scale Gaussian pyramid regards the situation as a whole, and then deals with the local details, At coarse scales, the global registration parameters are relatively easy to be estimated, and then the solution of the registration problem at one scale is the starting guess for the registration problem defined at the next finer scale, etc. The multi-scale representation may be combined with other methods to handle complex optimization problems.

Secondly, for medical image registration, especially US registration involved with strong speckle noise, it is a great challenge and difficult task, and only by improving algorithm to advance registration results

becomes harder and harder. Since it is hard for US de-noising, instead of only improving algorithm models to de-noise US, nano-materials are introduced to enhance the contrast and brightness of US, which is equivalent to de-noise US in a sense. In a word, it is feasible that novel nano-materials combined with excellent algorithm models are used to solve some difficult problems in medical image field. Nowadays, since it has become the bottleneck to only improve the algorithms for medical image registration, nano-materials could be introduced to enhance medical imaging, which will be beneficial to the following registration.

Lastly, for medical images processing (US-MRI registration included), algorithm modeling stage or images processing stage should not be only focused on, and attention must be paid to the imaging stage. High quality imaging is essential for follow-up work, and comparison experiments also demonstrate the above conclusions.

Funding Statement: This project is financially supported by Xuzhou's special funds for science and technology innovation (KC18008, 2018). Funding also partially comes from Jiangsu Overseas Visiting Scholar Program for University Prominent Young & Middle-aged Teachers and Presidents.

Conflicts of Interest: The authors declare that they have no conflicts of interest to report regarding the present study.

References

1. Yang, F., Zhang, M. A., He, W., Chen, P., Cai, X. W. et al. (2011). Controlled release of Fe₃O₄ nanoparticles in encapsulated microbubbles to tumor cells via sonoporation and associated cellular bioeffects. *Small*, 7(7), 902–910. DOI 10.1002/sml.201002185.
2. Cai, X. W., Yang, F., Gu, N. (2012). Applications of magnetic microbubbles for theranostics. *Theranostics*, 2(1), 103–112. DOI 10.7150/thno.3464.
3. Li, X. Y., Xia, S. J., Zhou, W., Ji, R., Zhan, W. W. (2019). Targeted Fe-doped silica nanoparticles as a novel ultrasound-magnetic resonance dual-mode imaging contrast agent for HER2-positive breast cancer. *International Journal of Nanomedicine*, 14, 2397–2413. DOI 10.2147/IJN.S189252.
4. Ali, L. M., Marzola, P., Nicolato, E., Fiorini, S., Heras Guillamon, M. D. L. et al. (2019). Polymer-coated superparamagnetic iron oxide nanoparticles as T₂ contrast agent for MRI and their uptake in liver. *Future Science OA*, 5(1). DOI 10.4155/fsoa-2017-0054.
5. Jung, E. M., Schreyer, A. G., Schacherer, D., Menzel, C., Farkas, S. et al. (2009). New real-time image fusion technique for characterization of tumor vascularisation and tumor perfusion of liver tumors with contrast-enhanced ultrasound, spiral CT or MRI: first results. *Clinical Hemorheology and Microcirculation*, 43(1–2), 57–69. DOI 10.3233/CH-2009-1221.
6. Schlaier, J. R., Warnat, J., Dorenbeck, U., Proescholdt, M., Schebesch, K. M. et al. (2004). Image fusion of MR images and real-time ultrasonography: evaluation of fusion accuracy combining two commercial instruments, a neuronavigation system and a ultrasound system. *Acta Neurochirurgica*, 146(3), 271–277. DOI 10.1007/s00701-003-0155-6.
7. Weaver, A. A., Nguyen, C. M., Schoell, S. L., Maldjian, J. A., Stitzel, J. D. (2015). Image segmentation and registration algorithm to collect thoracic skeleton semilandmarks for characterization of age and sex-based thoracic morphology variation. *Computers in Biology and Medicine*, 67, 41–48. DOI 10.1016/j.combiomed.2015.10.004.
8. Hong, H., Lee, J., Yim, Y. (2008). Automatic lung nodule matching on sequential CT images. *Computers in Biology and Medicine*, 38(5), 623–634. DOI 10.1016/j.combiomed.2008.02.010.
9. Bhuiyan, A., Karmakar, C., Kawasaki, R., Lamoureux, E., Ramamohanarao, K. et al. (2014). Retinal artery and venular caliber grading: a semi-automated evaluation tool. *Computers in Biology and Medicine*, 44, 1–9. DOI 10.1016/j.combiomed.2013.07.018.
10. Maureen, S. (2005). A guide to analysing tongue motion from ultrasound images. *Clinical Linguistics & Phonetics*, 19(6–7), 455–501. DOI 10.1080/02699200500113558.

11. Hou, M., Yang, M. Y., Yang, R. B., Ren, S. J., Wang, S. M. et al. (2019). Ultrasound-magnetic resonance imaging fusion scheme based on non-negative matrix factorization and dual modality contrast agent. *International Journal of Computational Methods*, 16(3), 1844001. DOI 10.1142/S0219876218440012.
12. Hou, M., Chen, C. X., Tang, D. L., Luo, S. H., Yang, F. et al. (2015). Magnetic microbubble-mediated ultrasound-MRI registration based on robust optical flow model. *Biomedical Engineering Online*, 14(Suppl 1), S14. DOI 10.1186/1475-925X-14-S1-S14.
13. Hou, M., Luo, S. H., Yang, F., Ruan, X. B., Gu, N. (2012). MRI-ultrasound registration based on dual modality contrast agent. *Chinese Science Bulletin (Chinese Version)*, 57(22), 2119–2126. DOI 10.1360/972011-2715.
14. Hou, M., Luo, S. H., Yang, F., Ruan, X. B., Gu, N. (2013). MRI-ultrasound fusion based on magnetic microbubble contrast agent (in Chinese). *Scientia Sinica (Informationis)*, 43(11), 1445–1459. DOI 10.1360/112012-664.
15. Yang, P., Luo, X. F., Wang, S., Wang, F., Tang, C. B. et al. (2017). Biodegradable yolk-shell microspheres for ultrasound/MR dual-modality imaging and controlled drug delivery. *Colloids and Surfaces B: Biointerfaces*, 151, 333–343. DOI 10.1016/j.colsurfb.2016.12.037.
16. Yang, P., Wang, F., Luo, X. F., Zhang, Y. T., Guo, J. et al. (2014). Rational design of magnetic nanorattles as contrast agents for ultrasound/magnetic resonance dual-modality imaging. *ACS Applied Materials & Interfaces*, 6(15), 12581–12587. DOI 10.1021/am502550b.
17. Guo, H. Z., Jiang, Z. Q., Song, S., Dai, T. T., Wang, X. Y. et al. (2016). Structural regulation of self-assembled iron oxide/polymer microbubbles towards performance-tunable magnetic resonance/ultrasonic dual imaging agents. *Journal of Colloid and Interface Science*, 482, 95–104. DOI 10.1016/j.jcis.2016.07.042.
18. Song, S., Guo, H. Z., Jiang, Z. Q., Jin, Y. Q., Wu, Y. et al. (2015). Self-assembled microbubbles as contrast agents for ultrasound/magnetic resonance dual-modality imaging. *Acta Biomaterialia*, 24, 266–278. DOI 10.1016/j.actbio.2015.06.025.
19. Morch, Y., Hansen, R., Berg, S., Aslund, A. K. O., Glomm, W. R. et al. (2015). Nanoparticle-stabilized microbubbles for multimodal imaging and drug delivery. *Contrast Media & Molecular Imaging*, 10(5), 356–366. DOI 10.1002/cmml.1639.
20. Wang, X., Niu, D. C., Li, P., Wu, Q., Bo, X. W. et al. (2015). Dual-enzyme-loaded multifunctional hybrid nanogel system for pathological responsive ultrasound imaging and T-2-weighted magnetic resonance imaging. *ACS Nano*, 9(6), 5646–5656. DOI 10.1021/nn5068094.
21. Xu, S. J., Yang, F., Zhou, X., Zhuang, Y. P., Liu, B. X. et al. (2015). Uniform PEGylated PLGA microcapsules with embedded Fe₃O₄ nanoparticles for US/MR dual-modality imaging. *ACS Applied Materials & Interfaces*, 7(36), 20460–20468. DOI 10.1021/acsami.5b06594.
22. Zheng, J. Z., Perkins, G., Kirilova, A., Allen, C., Jaffray, D. A. (2006). Multimodal contrast agent for combined computed tomography and magnetic resonance imaging applications. *Investigative Radiology*, 41(3), 339–348. DOI 10.1097/01.rli.0000186568.50265.64.
23. Kuznetsova, S., Grendarova, P., Roy, S., Sinha, R., Thind, K. et al. (2019). Structure guided deformable image registration for treatment planning CT and post stereotactic body radiation therapy (SBRT) Primovist® (Gd-EOB-DTPA) enhanced MRI. *Journal of Applied Clinical Medical Physics*, 20(12), 109–118. DOI 10.1002/acm2.12773.
24. Piskunowicz, M., Kosiak, W., Batko, T., Adamkiewicz-Drozynska, E., Szarmach, A. (2013). Intravenous ultrasound contrast agents vs. other imaging methods in pediatric patients with neoplastic diseases—a comparison. *Journal of Ultrasonography*, 13(55), 438–445. DOI 10.15557/JoU.2013.0047.
25. Duan, L., Yang, F., He, W., Song, L. N., Qiu, F. et al. (2016). A multi-gradient targeting drug delivery system based on RGD-L-TRAIL-labeled magnetic microbubbles for cancer theranostics. *Advanced Functional Materials*, 26(45), 8313–8324. DOI 10.1002/adfm.201603637.
26. Liu, Y., Yang, F., Yuan, C. X., Li, M. X., Wang, T. T. et al. (2017). Magnetic nanoliposomes as in situ microbubble bombers for multimodality image-guided cancer theranostics. *ACS Nano*, 11(2), 1509–1519. DOI 10.1021/acsnano.6b06815.
27. Gao, Z. Y., Gu, B., Lin, J. R. (2008). Monomodal image registration using mutual information based methods. *Image and Vision Computing*, 26(2), 164–173. DOI 10.1016/j.imavis.2006.08.002.

28. Abdullah, O. (2018). Convex optimization via symmetrical holder divergence for a WLAN indoor positioning system. *Entropy*, 20(9), 639. DOI 10.3390/e20090639.
29. Hernandez, M. (2017). Primal-dual convex optimization in large deformation diffeomorphic metric mapping: LDDMM meets robust regularizers. *Physics in Medicine & Biology*, 62(23), 9067–9098. DOI 10.1088/1361-6560/aa925a.
30. Zhang, T., Li, Y., Tong, J. W. (2017). An autonomous underwater vehicle positioning matching method based on iterative closest contour point algorithm and affine transformation. *Proceedings of the Institution of Mechanical Engineers, Part M: Journal of Engineering for the Maritime Environment*, 231(3), 711–722. DOI 10.1177/1475090216683310.
31. Dai, T., Miao, L. J., Shao, H. J., Shi, Y. S. (2019). Solving gravity anomaly matching problem under large initial errors in gravity aided navigation by using an affine transformation based artificial bee colony algorithm. *Frontiers in Neurorobotics*, 13, 60. DOI 10.3389/fnbot.2019.00019.
32. Wang, C., Shu, Q., Yang, Y. X., Yuan, F. (2018). Point cloud registration in multidirectional affine transformation. *IEEE Photonics Journal*, 10(6), 1–15. DOI 10.1109/JPHOT.2018.2876689.
33. Lee, Y. S., Hwang, W. L., Tian, X. L. (2015). Continuous piecewise affine transformation for image registration. *International Journal of Wavelets, Multiresolution and Information Processing*, 13(1), 1550006. DOI 10.1142/S021969131550006X.
34. Zhang, Z. X., Li, J. Z., Li, D. D. (2003). Research of automated image registration technique for infrared images based on optical flow field analysis. *Journal of Infrared and Millimeter Waves*, 22(4), 307–312.
35. Zhang, Z. X., Cui, P. Y. (2008). A reliable method of image registration based on optical flow field and feature extraction. *Chinese Journal of Electronics*, 17(1), 12–15.
36. Zhang, Y. J., Jing, Y. M., Liang, X. H., Xu, G. L., Dong, L. (2012). Dynamic lung modeling and tumor tracking using deformable image registration and geometric smoothing. *Molecular & Cellular Biomechanics*, 9(3), 213–226.
37. He, C. L., Wang, J. Q., Huang, Y. X., Zhu, T. J., Miao, Y. H. et al. (2016). The correlation between texture features and fibrous cap thickness of lipid-rich atheroma based on optical coherence tomography imaging. *Molecular & Cellular Biomechanics*, 13(1), 23–26.